Size-dependent magnetic properties of Mn-Co-NiO based heterostructured nanoparticles

Cite as: AIP Advances 13, 025209 (2023); https://doi.org/10.1063/9.0000583 Submitted: 03 October 2022 • Accepted: 18 November 2022 • Published Online: 02 February 2023

🧓 Farhan Ishrak, 🗓 Robert A. Mayanovic and 🗓 Mourad Benamara

COLLECTIONS

Paper published as part of the special topic on 67th Annual Conference on Magnetism and Magnetic Materials









ARTICLES YOU MAY BE INTERESTED IN

Temperature dependent intrinsic Gilbert damping in magnetostrictive FeCoSiB thin film AIP Advances 13, 025003 (2023); https://doi.org/10.1063/9.0000418

Introduction of VN underlayer and caplayer for preparation of Mn₄N(001) single-crystal thin film with perpendicular magnetic anisotropy

AIP Advances 13, 025110 (2023); https://doi.org/10.1063/9.0000572

Phase stability and coercivity in La₂Fe₁₄B magnet

AIP Advances 13, 025211 (2023); https://doi.org/10.1063/9.0000403





ARTICLE AIP Advances scitation.org/journal/adv

Size-dependent magnetic properties of Mn-Co-NiO based heterostructured nanoparticles

Cite as: AIP Advances 13, 025209 (2023); doi: 10.1063/9.0000583 Submitted: 3 October 2022 • Accepted: 18 November 2022 • **Published Online: 2 February 2023**









Farhan Ishrak, 1,a) D Robert A. Mayanovic, 1 D and Mourad Benamara 2 D



AFFILIATIONS

- Department of Physics, Astronomy and Materials Science, Missouri State University, Springfield, Missouri 65897, USA
- ²Institute for Nano Science and Engineering, University of Arkansas, Fayetteville, Arkansas 72701, USA

Note: This paper was presented at the 67th Annual Conference on Magnetism and Magnetic Materials.

a) Author to whom correspondence should be addressed: fi25s@missouristate.edu

ABSTRACT

In this work, we investigate the synthesis, along with the structural and magnetic properties, of novel Mn-Co-NiO-based heterostructured nanocrystals (HNCs). The objective is to develop novel, well-structurally ordered inverted antiferromagnetic (AFM) NiO-ferrimagnetic (FiM) spinel phase overgrowth HNCs. Inverted HNCs are particularly promising for magnetic device applications because their magnetic properties are more easily controlled by having well-ordered AFM cores, which can result in magnetic structures having large coercivities, tunable blocking temperatures, and other enhanced magnetic effects. The synthesis of the HNCs is accomplished using a two-step process: In the first step, NiO nanoparticles are synthesized using a thermal decomposition method. Subsequently, Mn-Co overgrowth phases are grown on the NiO nanoparticles via hydrothermal nanophase epitaxy, using a fixed pH level (~5.3) of the aqueous medium. This pH level was selected based on previous work in our laboratory showing that NiO/Mn₃O₄ HNCs of constant size have optimal coercivity and exchange bias when synthesized at a pH of 5.0. The crystalline structure and gross morphology of the Mn-Co-NiO-based HNCs have been analyzed using X-ray diffraction (XRD) and Scanning Electron Microscopy (SEM) techniques, respectively. Analysis using these techniques shows that the HNCs are composed of a NiO core and a CoMn₂O₄ overgrowth phase. Rietveld refinement of XRD data shows that the NiO core has the rocksalt (Fm3m) cubic crystal structure and the CoMn2O4 overgrowth has the spinel (I41/amd) crystal structure. Moreover, an increased relative amount of the CoMn₂O₄ overgrowth phase is deposited with decreasing NiO core particle size during the synthesis of the HNCs. The results from PPMS magnetization and high-resolution transmission electron microscopy (HRTEM) characterization of the Mn-Co-NiO-based HNCs are discussed herein.

© 2023 Author(s). All article content, except where otherwise noted, is licensed under a Creative Commons Attribution (CC BY) license (http://creativecommons.org/licenses/by/4.0/). https://doi.org/10.1063/9.0000583

INTRODUCTION

Due to their tunable magnetic properties, bimagnetic multicomponent nanoparticles in core-shell or decorated topology with antiferromagnetic (AFM) and ferro/ferromagnetic (FM/FiM) components have been the focus of extensive research. These magnetic heterostructured nanocrystals (HNCs) have potential for use in contemporary spintronic devices, magnetic random-access memory (MRAM) devices, drug delivery, ferrofluids, pigments, and hyperthermia.¹⁻⁴ AFM-based HNCs are highly promising for spintronic device applications because they do not lose their memories,

can process data faster, can be made smaller, and use less power.^{5,6} Transition metal oxides such as CoO, Cr₂O₃, MnO, and NiO have been widely used as AFM components because they allow the magnetic properties of HNCs to be tuned, including fast switching times between spin states, weak interparticle relations, and overcoming the superparamagnetic limit. Additionally, AFM materials are capable of sub-picosecond magnetization switching, which can help FM/FiM based magnetic recording devices overcome their switching rate constraint. 9-11 Furthermore, the FM-AFM interface exhibits a strong exchange coupling interaction with a high exchange bias (EB) effect (hysteresis loop shift or coercivity enhancement in

the field-cooled condition). In bimagnetic core-shell type HNCs, the combination of AFM and FM/FiM components results in improved spin-transfer torque, terahertz oscillation, and exchange bias effect. 12-14 Utilizing an AFM component such as NiO in magnetic HNCs is very advantageous since it enables the magnetic characteristics to be tuned. The EB effect comes from the fact that AFM anisotropy has a "pinning" effect on interface spins. This makes it harder to reverse the FM magnetization in the opposite direction of field cooling.¹⁵ High crystallinity in the AFM region, epitaxial shell development, and a greater AFM than FiM anisotropy are all favorable for EB. 16,17 Inverted core-shell nanoparticles (AFM core, FiM shell) provide improved control of AFM phase crystallinity and anisotropy.¹⁸ Magnetic HNCs' characteristics can be changed to suit particular purposes by utilizing various synthesis techniques, adjusting the pH, temperature, time length, and other synthesis factors, as well as by altering the quantity or kind of dopant in the core or shell. Because the synthesis procedures could regulate the surface, interface, and morphology of the nanoparticles, they have a direct affect on the properties of HNCs. In our lab, faceted and pseudospherical HNCs have been grown using the hydrothermal approach, and it has been discovered that in some cases they display significant exchange bias and coercivity. 19,20 Initial research in our lab has shown that NiO@Mn_xNi_{1-x}O@Mn₃O₄ HNCs may achieve high coercivity and exchange bias fields at low temperatures (5 K), and decent values are feasible at room temperature. 19-21 However, these works did not attempt HNC synthesis with bimetallic spinel phases. In this research, we aimed to synthesize magnetic HNCs using co-deposition of two different metal ions- Mn and Co. Keeping the molar concentration ratio at Mn:Co = 2:1, we synthesized a series of CoMn₂O₄ spinel shell/nanoisland coated NiO nanoparticles with different core particle size ranging from 9.31 nm to 24.52 nm. Furthermore, we address the structural, morphological, and magnetic characteristics of our NiO-CoMn₂O₄ HNCs.

EXPERIMENTAL METHODS

The synthesis of the HNCs involved two steps. The first step comprises the thermal decomposition of Ni(OH)₂ to form the NiO precursor, as per the process outlined by El Kemary et al.²² Absolute ethanol was used to dissolve 0.111 M of nickel chloride hexahydrate, which was then added to the solution along with hydrazine monohydrate. Sodium hydroxide solution was used to keep the pH around 12. Here, NiCl₂.6H₂O, N₂H₄.H₂O, and NaOH were used with a ratio of 1:5:10. The mixture was then stirred with a magnetic stirrer for 1.5 hours at room temperature. After the reaction product had been stirred, it was washed with deionized (DI) water to eliminate any remnants before being centrifuged in a solution of 50% ethanol. The resulting Ni(OH)2.0.5H2O nanoparticles were dried overnight at 50 °C and then heated to 600 °C for about two hours to completely dry and activate the thermal decomposition process. Here, the maximum decomposition temperature was 600 °C, where the decomposition time varied between 1 and 2 hours. Using the above procedure, core NiO nanoparticles were synthesized with diameters ranging from 9.31 nm to 24.52 nm. The size of the NiO nanoparticles may change depending on the temperature and time of thermal breakdown. Next, our previously established hydrothermal nanophase epitaxy procedure ^{5,23,24} was utilized to grow the Mn-

and Co-bearing oxide phases over the NiO core. First, MnCl₂.3H₂O and CoCl₂.6H₂O (2:1) were added to deionized water that had been purged with N2 for 15 to 20 minutes at a temperature between 70 and 80 °C. Drops of HCl or NaOH were used to modify the pH of the solution around 5. Previously, it was found in our lab that at pH values trending from low acidic to neutral, nanoparticles having enhanced magnetic properties and the highest magnetization was found for HNCs synthesized at a pH of 5.0.21 Thus, we maintained the pH value of the hydrothermal solution at 5.06 to 5.3. Next, 0.33g of NiO nanoparticles were added to an aqueous solution containing 0.08M of Mn and Co salts. Following the addition of NiO nanoparticles to the Mn-Co chloride solution, the mixture was sonicated for 30 minutes before being placed in an autoclave. For the hydrothermal treatment, the autoclave was held in a furnace for 20 hours at a temperature of 200 °C. After the hydrothermal synthesis was complete, the product was centrifuged, rinsed with DI water, and then dried at 50 $^{\circ}$ C.

The HNC samples were analyzed for X-ray diffraction (XRD) at room temperature using a Bruker D8 Discover powder diffractometer (Bruker AXS, Karlsruhe, Germany) equipped with Cu K-a X-ray radiation of 1.541 84 wavelength. The instrument is operated at 40 kV and 40 milliamperes. The X-ray beam was focused using a Göbel mirror and an incident beam slit of 0.6 mm. A 1-D Si strip detector from Linxeye was used to measure the XRD spectra. The Rietveld refinement fitting of the XRD spectra measured from the samples was made utilizing the Burker TOPAS software. The background in the XRD patterns was modeled using a Chebychev polynomial of the fifth order. The SEM structural and morphological analysis was conducted using a 20 kV FESEM (FEI-Quantum 200) device. The SEM samples were prepared by sonicating very small amounts of nanoparticle powder in microcentrifuge tubes and dropping microliter amount of sample directly on the sample holder in a single layer. The sample was loaded into the chamber after the liquid was air-dried. Using SEM-EDS and a field emission gun (Oxford Instruments), a preliminary elemental study of the samples was made. For transmission electron microscopy (TEM), nanoparticle samples were dispersed in hexane via sonication. Drops of samples were deposited onto Cu lacey grids using micropipettes and dried for few minutes. TEM imaging was performed using a Titan 80-300 (FEI) with the 300 keV field emission gun. Fast Fourier transformation (FFT) algorithm within ImageJ software was used to generate simulated selected area electron diffraction pattern from high resolution TEMP (HRTEM) images. The magnetic measurements were made using a Quantum Design Physical Property Measurement System (PPMS). The samples were cooled to 5 K from room temperature in a field of 100 Oe for the FC curve, and the magnetization data were measured in a 100 Oe external field for the magnetization versus temperature data, both field-cooled (FC) and zero-field-cooled (ZFC) measurements. The FC and ZFC hysteresis curves were measured at varied intervals and at 5 K from -25 000 Oe to 25 000 Oe. For the FC M vs H hysteresis measurements, the samples were cooled in a field of 100 Oe.

RESULTS AND DISCUSSION

Figure S1 in supplementary material shows the XRD spectra measured from our samples of varying sized NiO nanoparticles, after deposition of the cobalt manganate (CoMn₂O₄) overlayer. Rietveld

TABLE I. List of samples with size.

Sample	A1	A2	A3	A4
Core Size (nm)	9.31	19.07	24.39	24.52
HNC Size	11.87	20.65	25.24	26.22

refinement was performed to determine the structure and phase proportion of shell and core materials. The presence of two separate phases in the samples is revealed using Rietveld refinement fitting of the XRD patterns: NiO and CoMn2O4, which is totally consistent with investigations of the NiO@Mn_xNi_{1-x}O@Mn₃O₄ HNCs made in our laboratory.²¹ The NiO core nanoparticles have a cubic rock-salt crystal structure with the space group Fm3m and the CoMn₂O₄ overgrowth has a spinel structure with the space group I4₁/amd. ^{25,26} The NiO cubic rocksalt phase contributes to the XRD pattern with reflections from (111), (200), (220), (311) and (222) diffracting planes at 37.5°, 43.55°, 63.18°, 75.76° and 79.75° peak positions, respectively. Similarly, the CoMn₂O₄ spinel structure phase contributes to the XRD pattern with (200), (211), (220), (312), (321), (400) and (305) reflection at peak position of 30.74°, 36.16°, 43.87°, 54.33°, 57.96°, 63.58° and 72.09°, respectively. Due to the proximity of peak positions and peak broadening, low intensity CoMn₂O₄ spinel peaks were dominated by higher intensity NiO peaks. The largest peak of the I41/amd CoMn2O4 structure, (211) at $2\theta \approx 36.2^{\circ}$ is visible in all the HNCs XRD spectra. As shown in the XRD spectra, sample A1 has the highest contribution (9.99%) from the CoMn₂O₄ overgrowth region which decreases in the higher core sized HNC samples. The associated goodness-of-fit (GOF) values given in the respective figures confirms the fitting of the peaks. The Scherrer formula $D = k\lambda/\beta\cos\theta$ was used to determine the crystallite size of the samples from the XRD data shown

Figure S2(a) shows an SEM image of agglomerated heterostructured nanoparticles. The elemental mapping of the agglomeration is shown in Figs. S2(b)–(f). The mapping shows uniform dispersion of Ni, Mn, Co, and O atom throughout the sample. The SEM-EDS linescan and distribution data, shown in Figs. S2(i) and S2(g), respectively, further confirms the presence of the constituent atoms in a single line across the sample.

Figure 1(a) shows a low-resolution TEM image of sample A3 depicting the morphology of the nanoparticles. Here, we see presence of faceted as well as pseudospherically shaped nanoparticles. The findings are consistent with previous work from our laboratory, 20,21,27 which observed a similar morphology for various HNC samples. A histogram plot of particle size distribution is shown in Fig. 1(b), determined from low resolution TEM imaging, giving an average particle size of 25.64 nm for sample A3. This is in very good agreement with our XRD Scherrer equation analysis yielding a particle size of 25.24 nm. HRTEM image analysis shown in Fig. 1(c) reveals the presence of NiO core and CoMn $_2$ O $_4$ overgrowth phases.

The temperature dependence of the FC and ZFC magnetization (M) curves measured as a function of temperature (T) are shown in Fig. S3 of supplementary material. The ZFC curves increase from an initial negative magnetization value, reach a peak, and then approach the FC curves at temperatures above ~200 K. The magnetic effects shown result from the powder sample's inherent magnetic characteristics and, possibly, the interparticle dipolar interactions.

Our nanoparticles were tightly packed for M-T measurements where interparticle dipolar interactions may occur and they have a finite size distribution. Thus, -d(FC-ZFC)/dT plotted vs temperature was used to determine the mean blocking temperature (T_B) for a measurement field of 100 Oe. 28 Sample A1 and A4 have most closely aligned blocking temperatures of 195 K and 198 K respectively which may be attributed to their high proportion of $CoMn_2O_4$ spinel counterparts. Sample A2 has a blocking temperature of 101 K whereas the T_B of sample A3 could not be determined from the experimental data.

Low temperature (5 K) magnetization vs magnetic field hysteresis data (M-H loops), for the ZFC condition are presented in Fig. 2. The coercivity ($H_{\rm C}$), remnant magnetization ($M_{\rm R}$), saturation magnetization ($M_{\rm S}$), and exchange bias field ($H_{\rm E}$) values derived from the hysteresis data are shown in Table II. For each sample, the hysteresis loops display the standard letter "S" shape although the shape for sample A2 trends slightly more toward an oval shape.

Compared to ZFC curves, the FC hysteresis loops in Fig. S4 are skewed along the positive M-axis direction and the negative H-axis (H_E) orientation, showing substantial exchange bias fields for

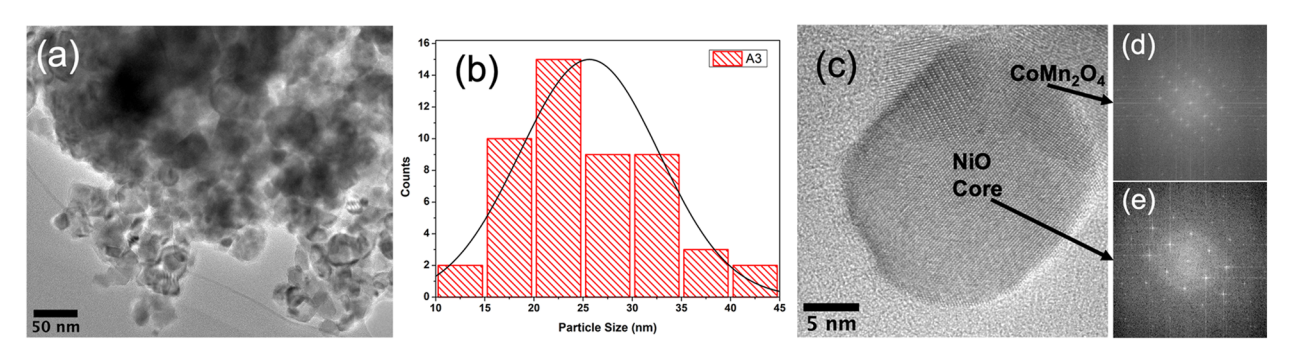


FIG. 1. (a) Low resolution TEM image of sample A3; (b) particle size distribution of sample A3 histogram plot; (c) HRTEM image of sample A1; (d,e) FFT images of CoMn₂O₄ shell/nanoisland and NiO core

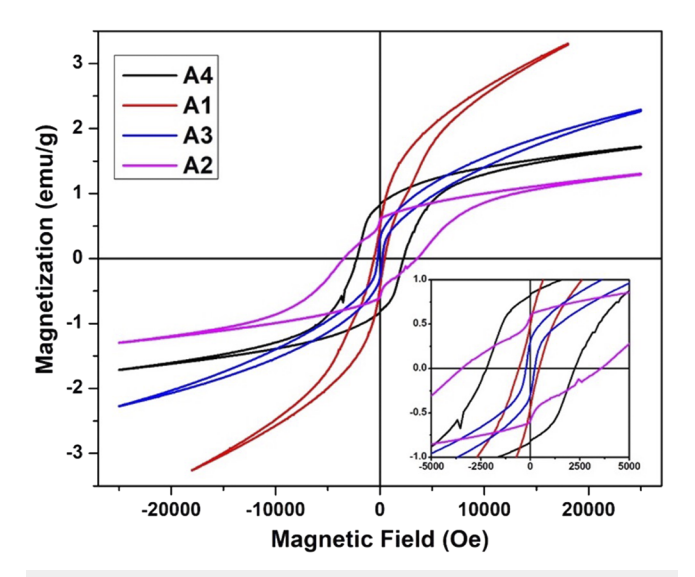


FIG. 2. Magnetization (M) vs Magnetic Field (H) curves for sample A4, A1, A3, and A2 (inset: magnified M-H loop).

our HNC samples. Vertical shifts in the FC M-H loops of Fe/Fe₂O₃ and Ni/NiO core-shell nanoparticles have been attributed by Zheng et al.²⁹ and He et al.,³⁰ respectively, to frozen spins at the surface of the AFM metal oxide layer. Larger M values result for the loop measured in the positive field direction because this aligns with the orientation of the FC field and the orientation of the frozen surface spins. The frozen Ni spins at the surface and/or interface of the NiO AFM core of our magnetic HNCs are responsible for the vertical shift of the FC M-H loops measured from our samples. Moreover, disorder effects at the surface and/or interface of the NiO core cause the frozen spins. At the interface between the AFM-FiM phases, the frozen Ni spins in the NiO core and the Mn spins from the CoMn₂O₄ overlayer are mainly uncompensated by most likely misfit dislocations, vacancies, stacking faults, and other defects.³¹ The data in Table II indicate that the smaller-sized samples (A1 and A2) have the largest exchange bias field values. Assuming sample A3 is anomalous, the trend indicates a maximal effect in H_E occurring for sample A2.

In Fig. S5, coercivity and retentivity are plotted as functions of the core size of the HNCs. Using the same assumption, we see a similar maximal effect for the coercivity $H_{\rm C}$ trend for the HCNs. There is no clear trend of the retentivity value with either the overall size or net size of the overgrowth of the HCN samples: the highest

TABLE II. Magnetic data from M-H loop analysis.

Sample	A1	A2	A3	A4
Retentivity, M _R (emu/g)	0.49	0.59	0.30	0.83
Coercivity, H _C (Oe)	577.7	3467.27	229.74	2215.15
Exchange Bias, H _E (Oe)	871.02	1480.01	159.24	473.62

M_R value, as shown in Table II and Fig. S5, is found for the largest-sized sample, A4. It is likely that in addition to the uncompensated spins, the frozen AFM spins also contribute to the exchange bias effect in our magnetic HNCs. In addition to the spin-spin interactions, domain structure, morphology, and spin clustering may be critical for manifesting magnetic HNC magnetic characteristics. Nevertheless, further study is required to fully understand the magnetic effects exhibited by our HNC samples.

CONCLUSIONS

Novel NiO/CoMn₂O₄ HNCs were synthesized for the first time by following a two-step synthesis procedure: the NiO core was produced using the thermal decomposition method and the CoMn₂O₄ overlayer of the HNCs was synthesized using a hydrothermal method. The crystal structure and the size distribution of both the NiO NPs, prior to overlayer growth, and the HNCs were determined using fitting of XRD spectra. Additionally, the TEM analysis confirms the overgrowth structure. The results of hysteresis loop measurements show that there is both a horizontal, due the exchange bias effect, and a vertical shift of the FC versus the ZFC curve at 5 K. The magnetization versus temperature measurements in the zero field (ZFC) condition reveals that the blocking temperatures for the HNCs vary from 101 K (A2) to 195 K (A1) and 198 K (A4). Excluding the results for sample A3, we observe a maximal effect versus overall size at ~21 nm (A2) for both the exchange bias field (H_E) and for the coercivity H_C, for the HCNs. The largest retentivity value (0.83 emu/g) was measured for the largest-sized sample (A4).

SUPPLEMENTARY MATERIAL

See supplementary material for XRD spectra, SEM images, magnetization vs temperature curves, magnetization vs magnetic field curves.

ACKNOWLEDGMENTS

The PPMS measurements were performed at the Cornell Center for Materials Research Shared Facilities, which are supported through the NSF MRSEC program (DMR-1719875).

AUTHOR DECLARATIONS

Conflict of Interest

The authors have no conflicts to disclose.

Author Contributions

Farhan Ishrak: Conceptualization (equal); Investigation (equal); Methodology (equal); Visualization (equal); Writing – original draft (equal). Robert A. Mayanovic: Conceptualization (equal); Funding acquisition (equal); Supervision (equal); Writing – review & editing (equal). Mourad Benamara: Data curation (equal).

DATA AVAILABILITY

The data that support the findings of this study are available within the article and its supplementary material.

REFERENCES

- ¹A. López-Ortega, D. Tobia, E. Winkler, I. V. Golosovsky, G. Salazar-Alvarez, S. Estradé, M. Estrader, J. Sort, M. A. González, S. Suriñach, J. Arbiol, F. Peiró, R. D. Zysler, M. D. Baró, and J. Nogués, Journal of the American Chemical Society 132, 9398 (2010).
- ²R. Scarfiello, C. Nobile, and P. D. Cozzoli, Frontiers in Materials 3 (2016).
- ³Y. Wang, H. Zhang, E. Liu, X. Zhong, K. Tao, M. Wu, C. Xing, Y. Xiao, J. Liu, and Y. Long, Advanced Electronic Materials 4, 1700636 (2018).
- ⁴N. J. Borys, M. J. Walter, J. Huang, D. V. Talapin, and J. M. Lupton, Science **330**, 1371 (2010).
- ⁵M. D. Hossain, R. A. Mayanovic, R. Sakidja, M. Benamara, and R. Wirth, Nanoscale **10**, 2138 (2018).
- ⁶M. Ghosh, K. Biswas, A. Sundaresan, and C. N. R. Rao, J. Mater. Chem. **16**, 106 (2006).
- ⁷A. B. Shick, S. Khmelevskyi, O. N. Mryasov, J. Wunderlich, and T. Jungwirth, Phys. Rev. B **81**, 212409 (2010).
- ⁸N. Thielemann-Kühn, D. Schick, N. Pontius, C. Trabant, R. Mitzner, K. Holldack, H. Zabel, A. Föhlisch, and C. Schüßler-Langeheine, Phys. Rev. Lett. **119**, 197202 (2017).
- ⁹S. Wienholdt, D. Hinzke, and U. Nowak, Physical Review Letters 108, 1 (2012).
- ¹⁰ A. V. Kimel, A. Kirilyuk, P. A. Usachev, R. V. Pisarev, A. M. Balbashov, and T. Rasing, Nature 435, 655 (2005).
- ¹¹T. Satoh, S. J. Cho, R. Iida, T. Shimura, K. Kuroda, H. Ueda, Y. Ueda, B. A. Ivanov, F. Nori, and M. Fiebig, *Physical Review Letters* **105**, 1 (2010).
- ¹² M. Ślęzak, T. Ślęzak, P. Dróżdż, B. Matlak, K. Matlak, A. Kozioł-Rachwał, M. Zając, and J. Korecki, Scientific Reports 9, 1 (2019).
- ¹³ M. Estrader, A. López-Ortega, S. Estradé, I. V. Golosovsky, G. Salazar-Alvarez, M. Vasilakaki, K. N. Trohidou, M. Varela, D. C. Stanley, M. Sinko, M. J.

- Pechan, D. J. Keavney, F. Peiró, S. Suriñach, M. D. Baró, and J. Nogués, Nature Communications 4, 1 (2013).
- ¹⁴J. Nogués, J. Sort, V. Langlais, V. Skumryev, S. Suriñach, J. S. Muñoz, and M. D. Baró, Physics Reports 422, 65 (2005).
- ¹⁵J. Nogués and I. K. Schuller, Journal of Magnetism and Magnetic Materials 192, 203 (1999).
- ¹⁶J. Nogués, V. Skumryev, J. Sort, S. Stoyanov, and D. Givord, Physical Review Letters 97, 157203 (2006).
- ¹⁷G. Margaris, K. N. Trohidou, and J. Nogués, Advanced Materials 24, 4331 (2012).
- ¹⁸M. Vasilakaki, K. N. Trohidou, and J. Nogués, Scientific Reports 5, 9609 (2015).
- 19 S. Hasan, R. A. Mayanovic, and M. Benamara, AIP Advances 8, 056305 (2018).
- ²⁰S. Hasan, R. A. Mayanovic, and M. Benamara, MRS Advances 2, 3465 (2017).
- ²¹ A. A. Shafe, M. D. Hossain, R. A. Mayanovic, V. Roddatis, and M. Benamara, ACS Applied Materials & Interfaces 13, 24013–24023 (2021).
- ²²M. El-Kemary, N. Nagy, and I. El-Mehasseb, Materials Science in Semiconductor Processing 16, 1747 (2013).
- ²³S. Dey, M. D. Hossain, R. A. Mayanovic, R. Wirth, and R. A. Gordon, J. Mater. Sci. 52, 2066 (2017).
- ²⁴M. D. Hossain, R. A. Mayanovic, R. Sakidja, and M. Benamara, Journal of Materials Research 32, 269 (2017).
- ²⁵J. L. Martin de Vidales, E. Vila, R. M. Rojas, and O. Garcia-Martinez, Chem. Mater. 7, 1716 (1995).
- ²⁶E. Vila, R. M. Rojas, J. L. Martín de Vidales, and O. García-Martínez, Chem. Mater. 8, 1078 (1996).
- ²⁷M. D. Hossain, R. A. Mayanovic, R. Sakidja, M. Benamara, and R. Wirth, Nanoscale **10**, 2138 (2018).
- ²⁸J. C. Denardin, A. L. Brandl, M. Knobel, P. Panissod, A. B. Pakhomov, H. Liu, and X. X. Zhang, Phys. Rev. B 65, 064422 (2002).
- ²⁹ R. K. Zheng, G. H. Wen, K. K. Fung, and X. X. Zhang, Journal of Applied Physics 95, 5244 (2004).
- ³⁰ X. He, Y. Xu, X. Yao, C. Zhang, Y. Pu, X. Wang, W. Mao, Y. Du, and W. Zhong, RSC Advances **9**, 30195 (2019).
- ³¹E. Lottini, A. López-Ortega, G. Bertoni, S. Turner, M. Meledina, G. Van Tendeloo, C. de Julián Fernández, and C. Sangregorio, Chemistry of Materials 28, 4214 (2016)